Journal of Industrial and Engineering Chemistry 72 (2019) 107–116

Contents lists available at ScienceDirect

Journal of Industrial and Engineering Chemistry

journal homepage: www.elsevier.com/locate/jiec

Designing metal oxide-vertical graphene nanosheets structures for 2.6 V aqueous asymmetric electrochemical capacitor

Subrata Ghosh[a,*], S.R. Polaki[b], Gopinath Sahoo[b], En-Mei Jin[a], M. Kamruddin[b], Jung Sang Cho[c], Sang Mun Jeong[a,*]

[a] Department of Chemical Engineering, Chungbuk National University, 1 Chungdae-ro, Seowon-Gu, Cheongju, Chungbuk 28644, Republic of Korea
[b] Surface and Nanoscience Division, Materials Science Group, Indira Gandhi Centre for Atomic Research-Homi Bhabha National Institute, Kalpakkam, Tamil Nadu 603102, India
[c] Department of Engineering Chemistry, Chungbuk National University, 1 Chungdae-ro, Seowon-Gu, Cheongju, Chungbuk 28644, Republic of Korea

ARTICLE INFO

Article history:
Received 17 October 2018
Received in revised form 23 November 2018
Accepted 5 December 2018
Available online 7 December 2018

Keywords:
Graphene
Metal oxides
Electrochemical capacitor
PECVD
Hydrothermal

ABSTRACT

The asymmetric electrochemical capacitor was realized by MnO_2/Vertical graphene nanosheets (VGN) and Fe_2O_3/VGN as positive and negative electrodes, respectively. The surface of VGN skeleton is independently decorated with MnO_2 having sponge gourd-like morphology and Fe_2O_3 having nanorice like morphology. Both the electrodes have shown around 250 times higher charge-storage capacity than the bare VGN (0.47 mF/cm^2) with the specific capacitance of 118 (MnO_2/VGN) and 151 mF/cm^2 (Fe_2O_3/VGN). The fabricated asymmetric device exhibited a specific capacitance of 76 mF/cm^2 and energy density of 71 μWh/cm^2 with an excellent electrochemical stability up to 12,000 cycles, over a potential window of 2.6 V.

Introduction

With the ever-rising proliferation of portable and flexible energy storage devices, an electrochemical capacitor (EC) have drawn the significant interest, owing to their higher power density and longer cyclic stability in comparison to the conventional batteries [1,2]. However, their major drawback is low energy density compared to the conventional batteries, which limits their commercialization on a large scale. The phase space available to enhance the energy density is spanned by two major elements — the electrode material and the electrolyte [1,2]. An electrolyte with higher potential window and dielectric constant is found to enhance the energy density [3]. Since the electrode–electrolyte interactions play a major role, it is important to engineer the electrode materials, such that the increase in effective energy density is quite significant [4].

Recently, carbon nanostructures and 2D materials have been widely studied as EC electrode materials, followed by the transition metal oxides/nitrides (TMO/N) or hydroxides and conducting polymers [1,5–11]. However, the use of a binder, issue of restacking and agglomeration during electrode fabrication are observed to lower the effective surface area and increase the internal resistance thereby limiting the power density. Therefore, vertically oriented self-supporting structures have drawn a significant attention in various context includes field emission, thermal management, sensors, energy and application etc. [12–16]. Vertical graphene nanosheets (VGN) are one of the beneficial architectures of 2D materials often referred to as carbon nanowalls, graphitic petals or few layered graphene nanoflakes. The VGN is an interconnected open porous network of vertically standing few-layer graphene sheets [17]. Owing to its compatibility with electrode materials and superiority compared to other conventional electrodes in all aspects, yet its specific capacitance in the range of microfarad/cm^2 to few millifarad/cm^2 only [4,18]. Apart from the double layer capacitance contribution, VGN also holds a promise to serve as a mechanical backbone of electrochemical capacitor electrode materials as well as provides conductive channels and multiple pathways for the electron and ion transport [19]. On the other hand, transition metal oxides (TMO) are often encouraging due to their higher theoretical capacitance even ten to hundred times higher than that of the carbon materials [7,20]. To overcome the flaws of pseudocapacitors like poor electrical conductivity and inferior electrochemical stability of TMO, an amalgamation of TMOs with carbon matrix is the traditional roadmap for the researchers. Noteworthy

* Corresponding authors.
E-mail addresses: subrataghosh.phys@gmail.com (S. Ghosh), smjeong@chungbuk.ac.kr (S.M. Jeong).

https://doi.org/10.1016/j.jiec.2018.12.008
1226-086X/

that the vertically oriented structure is more beneficial as energy storage electrode compared to its horizontal counterpart owing to the higher accessible surface area, larger edge density and multiple channels. Therefore, metal oxide coating on the vertically oriented carbon skeleton is an advantageous strategy to obtain a high-performance energy storage device. Furthermore, widening the potential window of electrolyte and in-turn increasing the energy density via the relation, $E = 0.5\,CV^2$ is a key challenge for the energy research community. Although usage of the organic electrolyte is capable in providing the higher potential window than the aqueous electrolyte, they are costly, toxic, flammable and lower ionic conductivity. In addition, the specific capacitance of electrode materials in aqueous electrolyte were found to 40–50% higher than that in organic media [21]. In this context, chemical activation of the electrode materials, use of novel electrolyte, fabrication of asymmetric electrochemical supercapacitor (ASC) device are the promising approaches to enhance the electrolyte–electrode interaction, widening potential window and hence the energy density [22–25]. However, the maximum reported potential window for aqueous ASC is limited within 1.6–2.0 V [26–31] and countable reports exhibited an aqueous ASC device with a potential window higher than 2 V [22,32,33]. In order to obtain ASC device with highest possible potential window, one should choose a proper pair of TMOs since the potential window also depends on the difference in work-function between the electrodes. Amidst TMOs, MnO_2 and Fe_2O_3 nanostructures are more popular, due to their higher capacity, abundances, low cost, non-toxicity and environment-friendly [27,29]. Inspite of the significant progress in architecting MnO_2 and Fe_2O_3 electrode that has been accomplished in SC performance, the complex fabrication process, cost, agglomeration and limited electrochemical performance hindered scaling-up its production. Hence, our scientific research has been focused towards designing a self-standing TMO- vertical graphene hybrid structure via an easy and facile method to construct a high voltage ASC device.

Herein, we constructed an aqueous based asymmetric electrochemical capacitor device comprised of binder-free and additive free, MnO_2/VGN and Fe_2O_3/VGN nanoarchitectures as the positive and negative electrode, respectively. We propose a facile and scalable method to prepare the sponge gourd-like MnO_2 and nanorice-like Fe_2O_3 structures onto each sheet of vertical graphene with preserving vertical orientation and open network, without the aid of binder and the conductive agent. The fabricated device ensured its ability to operate with the high cell voltage of 2.6 V in 1M sodium perchlorate electrolyte ($NaClO_4$). In a combination of open network and vertical orientation, metal oxide-VGN provides efficient accessible surface area and conductive pathways for the electrolyte ions. The advantages of such devices include an enhanced capacitance of 76 mF/cm^2, excellent stability and higher energy density.

Experimental method

Electrode fabrication

Vertical graphene growth

The VGN was grown using plasma enhanced chemical vapour deposition on the graphite paper substrate. The details of the growth process were elaborated in our previous report [34]. Briefly, the PECVD chamber was evacuated to 10^{-6} mbar pressure using the turbo-molecular pump. The temperature of the substrate was raised to 800 °C. Prior to the growth, the substrate was cleaned by Ar (20 sccm) plasma for 10 min. Thereafter, CH_4 (5 sccm) was fed into the chamber at the same temperature. The microwave plasma of 375 W was used to create the plasma and it has been maintained for the 4 h growth. Followed by the growth, the sample was annealed for 30 min at the same temperature by putting off the plasma power and gas flow. Finally, the VGN was cooled down naturally and taken out from the chamber for further experiment. The morphology and height of the VGN were shown in Fig. S1a and b, respectively. The VGN was used as a template for the growth of MnO_2 and Fe_2O_3 through the wet-chemistry and hydrothermal method, respectively, which were later used as the positive and negative electrode materials of the asymmetric device. In order to fabricate the metal oxide/VGN composites, firstly the as-prepared VGN were subjected to KOH treatment at 100 °C for 30 min to achieve better graphitic quality, wetting property and hence its electrochemical capacitor performance [23,35]. The contact angle measurements revealed the reduction in wetting angle from 110° to 76° (Fig. S1c–d), which was much less than our previous reported value [23].

Metal oxide-vertical graphene growth

The fabrication of MnO_2/VGN and the bare MnO_2 electrode was achieved by dip-coating followed by annealing at 400 °C. Briefly, the precursor solution of MnO_2 nanostructure was prepared by dissolving $KMnO_4$ in deionized water under constant magnetic stirring. An activated VGN was dipped into the $KMnO_4$ solution and consecutively subjected to keep the solution at 80 °C for 30 min. Subsequently, after the growth, the electrode was rinsed in DI water and ethanol. Finally, the samples were loaded into the furnace and allowed them to anneal for 2 h at 400 °C in Ar environment (Scheme 1). The growth of MnO_2 nanostructures on VGN occurred via the following reaction:

$$KMnO_4(aq.) + C(s) + H_2O^2 \rightarrow MnO_2(s) + CO_3^{2-} + HCO_3^- \quad (1)$$

The bare Fe_2O_3 nanorice was fabricated by hydrothermal methods to compare its performance with that of Fe_2O_3/VGN [36]. The graphite paper and activated VGN were immersed into

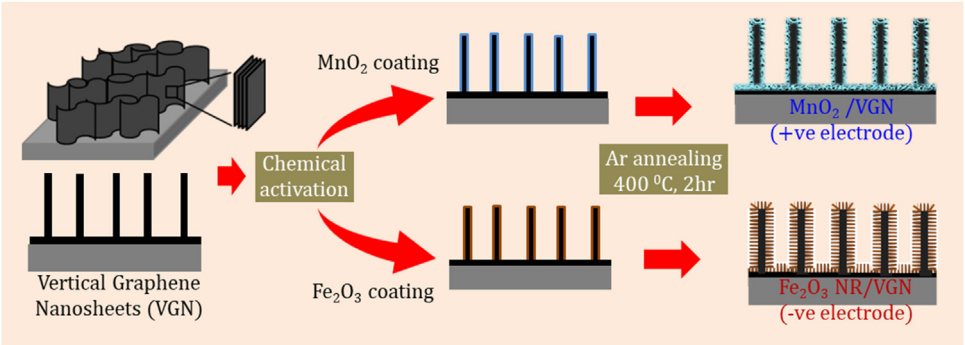

Scheme 1. Schematic of the fabrication process of positive and negative electrodes based on metal oxide-vertical graphene nanosheets.

$FeCl_3{\cdot}6H_2O$ ethanol/aqueous precursor solution to prepare a bare Fe_2O_3 nanorices and Fe_2O_3/VGN, respectively. The volume ratio of ethanol/aqueous was maintained at 1:1. Following which, the mixture was hydrothermally treated for 2 h at 120 °C using the Teflon-lined autoclave. Samples were taken out, washed by distilled water and ethanol several times. The VGN was uniformly coated with a yellow product of FeOOH. Before subjected to anneal, the composites were dried. Then the samples were loaded into the furnace and annealed for 2 h at 400 °C in Ar environment to achieve Fe_2O_3 nanorices structure (Scheme 1). The chemical reaction involved in the hydrothermal and subsequent annealing steps are

$$FeCl_3(aq.) \rightarrow Fe^{3+}(aq.) + 3(OH)^- \rightarrow FeOOH \rightarrow \alpha Fe_2O_3 + 3H_2O \quad (2)$$

Morphological and structural characterization

The morphology of as-grown and metal oxide decorated VGN was inspected using Field Emission Scanning Electron Microscope (FESEM, Zeiss, ULTRA PRUS). The wettability of all the studied samples was measured by water contact angle measurement using the sessile drop method (GSM, Surfacetech Co., Ltd.). The structural confirmation of all samples was investigated by Raman Spectroscopy (in-Via Renishaw) using 532 nm laser. The chemical composition and oxidation states were evaluated using X-Ray Photoelectron Spectroscopy (XPS, Thermo Scientific, K-Alpha) with Al K_α (1486.7 eV) X-ray radiation.

Electrochemical investigation

The electrochemical performance of each individual electrode was evaluated by cyclic voltammetry at different scan rates and charge–discharge at different current densities. The specific capacitance of electrodes (C_s) in F/cm^2 were estimated by the relations

$$C_s = \frac{\int IdV}{2 \times A \times \nu \times \Delta V} \quad (3)$$

$$C_s = \frac{I \times t_d}{A \times \Delta V} \quad (4)$$

where $\int IdV$,A, ν, ΔV and $t_d$are the area under the CV profile, exposed area of the electrode in electrolyte, scan rate, the operating potential window and discharge time, respectively. The individual electrodes were tested in the three-electrode configuration in which graphite rod and Ag/AgCl (Saturated in 3 M KCl) were used as the counter and reference electrodes, respectively. The supercapacitive behavior of asymmetric device was evaluated in the two-electrode configuration. To assemble the ASC device, $NaClO_4$ soaked filter paper as separator-cum-electrolyte was sandwiched between the electrodes. Autolab electrochemical workstation (AUT84455, Netherland) was employed for the above investigations. The specific energy density (Wh/cm^2) and power density (W/cm^2) of ASC device were estimated from using the following relations:

$$E = {}^{Cs \times \Delta\Omega\Theta}/2 \times 3600 C_s \times \Delta V^2/ \quad (5)$$

$$\text{and } P = E \times 3600/t_d \quad (6)$$

where E and P are the specific energy density and power density, respectively.

Result and discussion

Morphology and characterization of MnO_2/VGN

A well-controlled MnO_2 structure on the VGN was obtained according to Scheme 1 by varying the molar concentration of $KMnO_4$ precursor from 2 to 20 mM (Fig. S2). The well-controlled and uniform MnO_2/VGN was achieved only with the 10 mM $KMnO_4$ solution, where the open gap between the vertical nanosheets was preserved. The growth rate of the MnO_2 nanostructure can be controlled by immersion time and deposition temperature [37]. To compare the growth of MnO_2 on VGN, bare MnO_2 nanostructures was also grown on graphite paper and shown in Fig. S3. It has seen that sponge-gourd like the structure of MnO_2 on VGN whereas non-uniform coating of MnO_2 is observed on graphite paper (Fig. 1(a) and S3). The inset at the left-bottom of Fig. 1(a) and Fig. S1(a–b) demonstrates the porous morphology of VGN, where the vertically standing nanosheets are interconnected to each other and forms a porous interconnected network. The average inter-sheet spacing and thickness of each graphene sheet of VGN is measured by imageJ analysis and found to be 182 (±96) nm and 3–10 nm, respectively. The sponge gourd-like uniform and homogeneous coating of MnO_2 over the skeleton of VGN, without filling the intersheet-spacing is ensured from Fig. 1(a). The inter-sheet spacing and thickness of each sheet are varied from 56 to 141 nm and 54 (±12) nm, respectively after the MnO_2 decoration. In general, the inter-sheet spacing is considered as ion-reservoir and each vertical sheets serves as nanoelectrode [4]. This kind of morphology is beneficial for efficient ion-transport and effective accessibility for the full interior surface, which in-turn enhance the electrochemical performance.

The coating of MnO_2 onto VGN structure is confirmed by the Raman spectra and XPS analysis. The elemental confirmation of Mn, O and C of sponge-gourde like MnO_2/VGN and their distribution is shown in Fig. S4. The inset of Fig. 1b illustrates the presence of a weak band centred around 660 cm^{-1} corresponding to the Mn-O symmetric stretching vibration of MnO_6 octahedra [19,38]. The Raman spectra of MnO_2/VGN also consist of D″ (at 1100 cm^{-1}), D (at 1353 cm^{-1}), G (at 1586 cm^{-1}), D′ (1621 cm^{-1}), D+D″ (2464 cm^{-1}), G′ (2702 cm^{-1}), D+D′ (2946 cm^{-1}) and 2D′ (at 3237 cm^{-1}) peak. These peaks are characteristic Raman peaks of the VGN [39]. The presence of MnO_2 is also confirmed by XPS result of MnO_2/VGN (Fig. 1c). The survey spectrum is clear evidence for the presence of C, O and Mn. Fig. 1d. shows the deconvoluted C1*s* spectrum which includes sp^2-C at 284.4 eV, sp^3-C at 284.9, oxygenated C in C–O at 285.8 eV, C=O at 286.5 eV, –COO at 287.5, vacancy defect at 283.6 and π–π^* satellite peak at 292 eV [40]. These oxygenated functional groups can enhance the electrode wettability with the electrolyte and served as the bridging element for MnO_2. The high-resolution Mn2*p* peak, as shown in Fig. 1e, exhibited prominent Mn2$p_{3/2}$ and Mn2$p_{1/2}$ peaks with separation of 11.9 eV [41,42]. This result confirms the +4 oxidation state of Mn [33]. The deconvoluted high-resolution O1s spectra shows three distinct peaks at 526.7, 531.1 and 532.3 eV and are assigned as Mn–O–Mn, Mn–O–C and Mn–O–H, respectively (Fig. 1f) [43]. Wettability of the electrode materials is another influential factor to have better supercapacitive properties [44]. Noteworthy that, water is immediately spread once it drops onto the MnO_2/VGN surface. Whereas, the contact angle of MnO_2 surface was found to be in the range 26–77.9° in the literature [45]. The observed fact indicates that MnO_2/VGN is superhydrophilic in nature which may lend the excellent electrochemical capacitor performance. This hydrophilicity has arisen from the interaction between Mn–O–H group [46].

Morphology and characterization of Fe_2O_3/VGN

Fig. 2(a) displays the scanning electron micrographs of Fe_2O_3 nanorice decorated VGN. It is clear that Fe_2O_3 nanorice is grown on

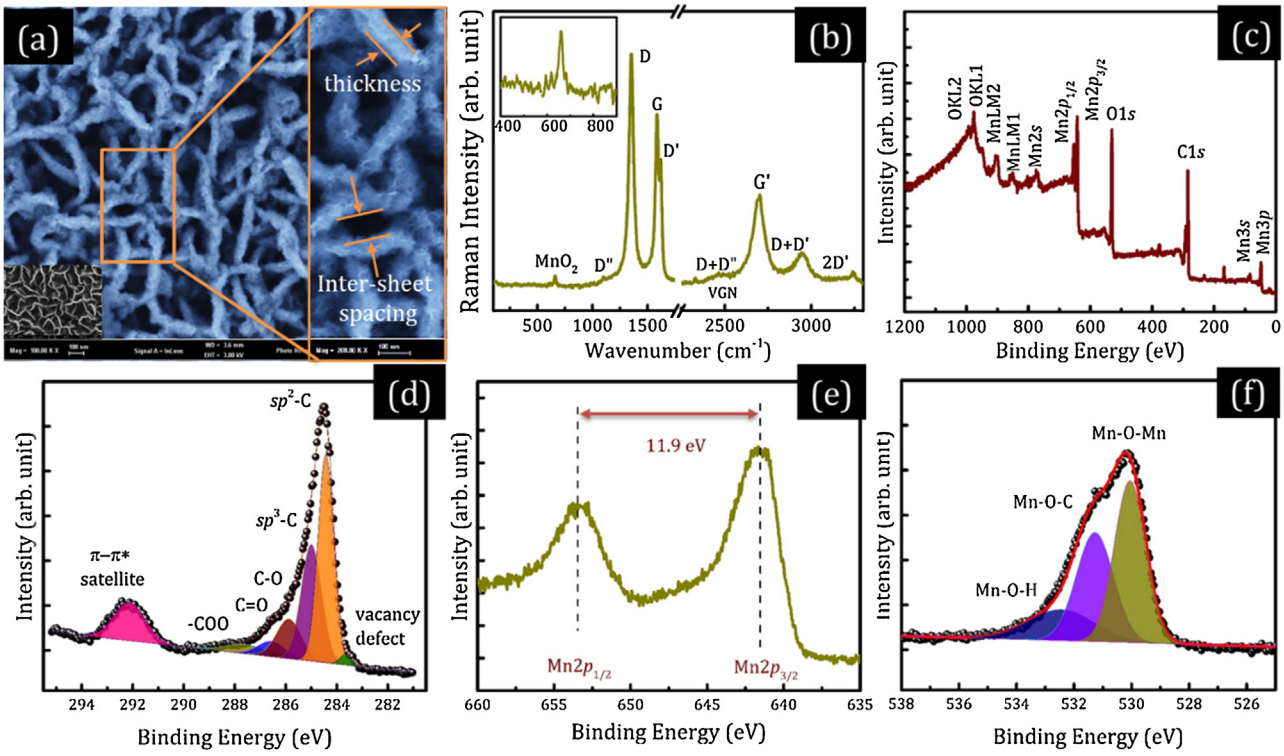

Fig. 1. (a) Micrograph with pristine VGN in insight, (b) Raman spectra, (c) X-ray photoelectron survey spectra; (d) high-resolution C1*s* spectra, (e) high-resolution Mn2*p* spectra and (f) high-resolution O1*s* spectra of MnO_2/VGN.

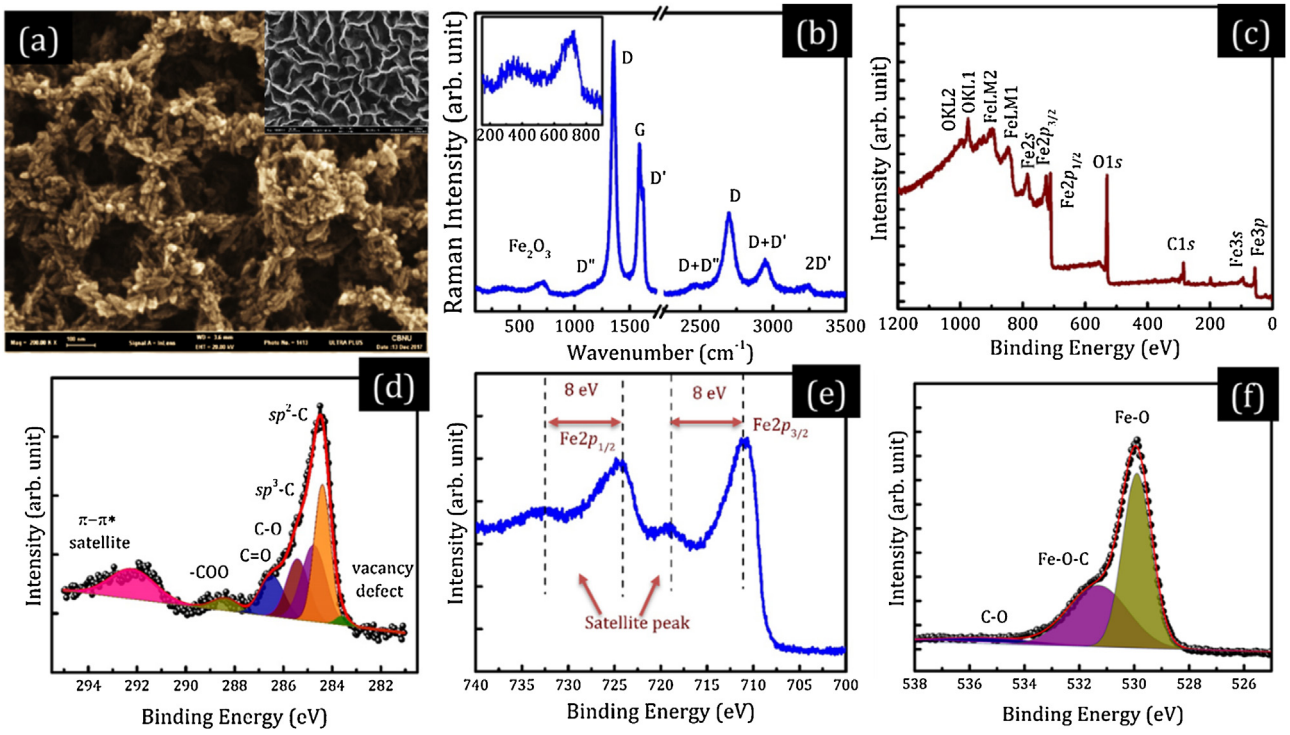

Fig. 2. (a) Micrograph with inset of as-prepared VGN, (b) Raman spectra, (c) X-ray photoelectron survey spectra, (d) high-resolution C1*s* spectra, (e) high-resolution Fe2*p* spectra and (f) high-resolution O1*s* spectra of Fe_2O_3/VGN.

the surface of VGN as well as on its edges. However, it is noteworthy to mention that the porous networked structure of VGN is well-maintained even after controlled Fe_2O_3 nanorice coating. The average length and diameter of nanorice are 30 to 74 nm and 18 (±2) nm, respectively. The average inter-sheet spacing and thickness of each sheet varied from 167 and 74 (±19) nm after Fe_2O_3 nanorice growth over VGN, respectively. To compare the growth of Fe_2O_3 nanorice on VGN, the bare Fe_2O_3 nanorice was grown on graphite paper. The morphology of bare Fe_2O_3 nanorice structures is depicted in Fig. S5. An agglomerated

and non-uniform Fe_2O_3 nanorices was observed on graphite paper. Whereas, non-agglomerated and uniform Fe_2O_3 nanorices are obtained while they were grown on VGN. This fact ensured the advantage of VGN as a mechanical platform to nurture uniform and homogeneous growth of hetero-nanostructures. However, the process parameters were well controlled and tuned to get Fe_2O_3 nanorices-VGN composites, while preserving the VGN geometry (Fig. S6). The Fe_2O_3/VGN composites were further evaluated by Raman spectroscopy and XPS. The Raman spectra of Fe_2O_3/VGN shows the characteristic peaks of both VGN and Fe_2O_3 (Fig. 2b). The inset of Fig. 2(b) shows the Raman spectra of Fe_2O_3. Two strong and broad peaks at 346 (T_1) and 718 cm^{-1} (A_1) have clearly appeared along with a very weak peak at 500 cm^{-1} (E) in Fig. 2(b). However, the magnon mode at 1300 cm^{-1} of Fe_2O_3 is overlapped with the D-peak of VGN [47]. The elemental confirmation was ensured from Fig. S7. Furthermore, the XPS measurement was carried out to evaluate the composition of the Fe_2O_3/VGN structure. The XPS survey spectrum exhibited C1*s* peak at 285 eV, and O1*s* peak at 530 eV accompanied with features of Fe_2O_3 (Fig. 2c–f). The high-resolution Fe2*p* spectra consists of Fe2$p_{3/2}$ peak at 710.9 eV and Fe2$p_{1/2}$ peak at 724.6 eV associated with their respective distinguishable satellite peaks at 718.9 and 732.6 eV (Fig. 2e). In conjunction, the binding energy difference between Fe2$p_{3/2}$ and its satellite peaks is around 8 eV [48]. Theg O1*s* spectrum of Fe_2O_3/VGN was deconvoluted into three components. The peaks at 529.9, 531.3 and 533 eV in the O1*s* spectrum are attributed to the Fe–O, Fe–O–C and C–O bond, respectively (Fig. 2f) [49]. Hence, the features observed in both Raman and XP spectra confirms the successful decoration of Fe_2O_3-nanorice structure onto the VGN matrix. Like MnO_2/VGN, the Fe_2O_3/VGN is also found to be super-hydrophilic in nature since water spread immediately once it drops on the surface.

Plausible formation mechanism of metal oxides on VGN

Based on the above investigation, we propose a step-wise formation mechanism of metal oxide/VGN as follows (Fig. 3). The growth mechanism of the VGN is already discussed in our previous reports [13,34]. The plasma-based growth of VGN is responsible due to the in-built electric field, competition between growth/etching process of carbon radicals, plasma density gradient towards the substrate and released strain at the grain boundary of nanoislands. Finally, the VGN formation takes place with partially terminated H-edges [34]. This terminated H-edges are replaced by more oxygenated function groups while they undergo KOH activation [23]. This oxygenated functional group serves as the nucleation centre for the TMO coating. In the next step of TMO coatings, oxygen group of metal oxides are reacting with active edges of VGN through replacement of H by metal ions or attaching with oxygen presence on the carbon surface. Finally, M–O–C formation occurs which leads to the successful coating of nanostructured metal oxides on VGN. The difference in morphology of both metal oxides is due to the procedure applied to grow individual metal oxide nanostructures.

Electrochemical performance of MnO_2/VGN

Prior to the electrochemical performance of the vertical metal oxide-graphene composite, the supercapacitive properties of VGN was evaluated. The cyclic voltammogram and charge–discharge profile of VGN are shown in Fig. S8(a–b). The estimated specific capacitance of VGN is found to 0.47 mF/cm^2 at a scan rate of 100 mV/s. Moreover, with the advantages of edges, high surface area and open network, the vertical structures are more efficient in charge-storage compared to planar graphitic structures [13]. A

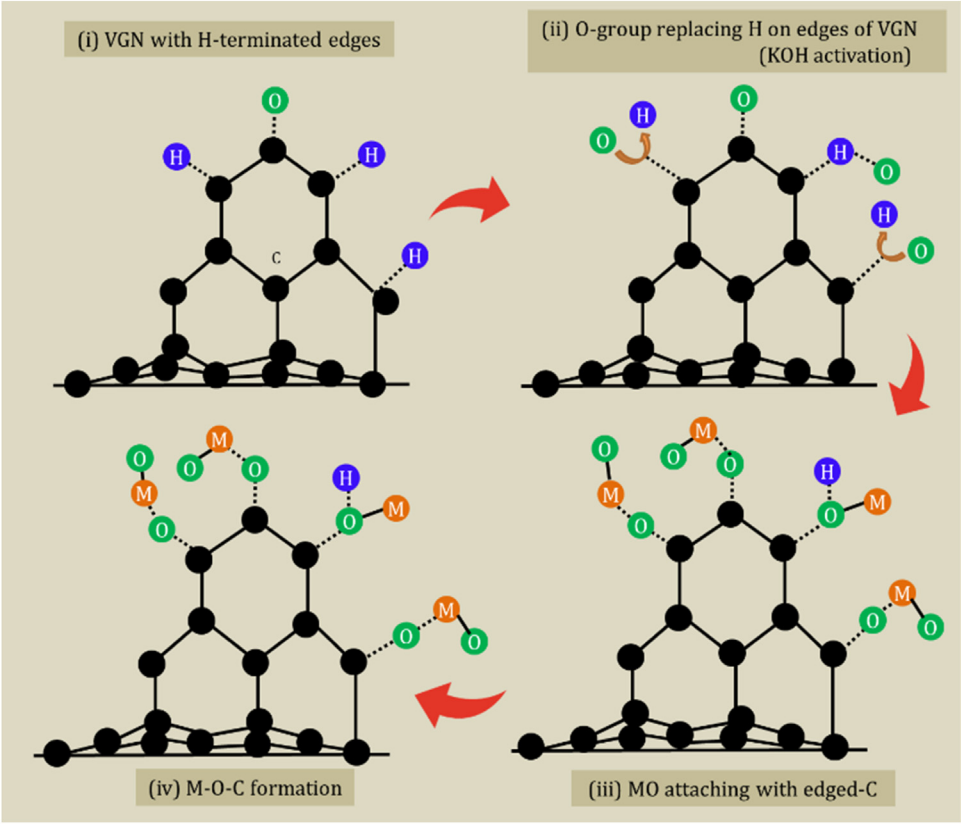

Fig. 3. Plausible formation scheme of vertical metal oxide-graphene composite (dotted lines corresponds to physical interactions among atoms).

near-rectangular and scan rate independent shape of CV assures the ideal capacitive behaviour of VGN. The electrochemical performance of MnO_2/VGN in the three-electrode system is displayed in Fig. 4. The quasi-rectangular, reversible and shape-preserved cyclic voltammogram with scan rate is observed from Fig. 4a. The absence of oxidation/reduction peak in CV ensures the faster reversible redox reaction of MnO_2. The comparative CV of MnO_2/VGN with VGN and bare MnO_2 ensures the higher charge storage capacity of MnO_2/VGN composite (Fig. 4b). In addition, it has shown that the bare MnO_2 and MnO_2/VGN can be safely operated up to 1.3 V in the positive window of potential (Fig. 4a). This fact is in well agreement with the existing report [43]. In addition, the increased area under the CV curve of bare MnO_2 is observed when the potential window is increased from (0–1.0 V) to (0–1.3 V). An enhanced CV area and therefore specific capacitance with respect to the applied potential window are due to the increased dielectric constant of electrolyte as well as reduced charge-separation distance [46]. The maximum specific capacitance of MnO_2/VGN is found to be 118 mF/cm^2 at 10 mV/s and maintained 35 mF/cm^2 while scan rate is increased by twenty times (Fig. 4c). The reduced specific capacitance of MnO_2/VGN at higher scan rate is due to the inability of complete redox transitions. Even, the charge-storage performance of MnO_2/VGN can be further enhanced by varying deposition time and temperature in $KMnO_4$ solution [37]. However, the obtained value is found to be higher than that of MnO_2 coated VGN (5.6 mF/cm^2 at 100 mV/s) [19], Mn–Mo oxide –CNTs composite (31 mF/cm^2 at 2 mV/s) [50], MnO_2 based composites (79.15 mF/cm^2 at 0.4 mA/cm^2) [51], MnO_2 coated carbon nanoparticles (109 mF/cm^2 at 5 mV/s) [52]. In order to evaluate the charge-storage behaviour, the current density with respect to scan rate is plotted in Fig. 4d. It is observed that the current density *vs* scan rate plot follows the power law relation: $i = av^b$. The value of b is determining factors for charge storage mechanism, wherein b = 1 corresponds to pure capacitive response and 0.5 refers to semi-infinite diffusion-controlled charge-storage. From the linear fitting, the slope is estimated to be 0.56, indicating the semi-infinite diffusion-controlled charge-storage mechanism of the MnO_2/VGN electrode (Fig. 4d). The charge-storage mechanism of MnO_2/VGN can be ascribed to the fast intercalation/de-intercalation of Na^+ ions into/out of the matrix and surface adsorption of Na^+ via following reactions, respectively [46]

$$MnO_2 + Na^+ + e^- \leftrightarrow MnooNA \quad (7)$$

$$(MnO_2)_{surface} + Na^+ + e^- \leftrightarrow (MnO_2^- Na^+)_{surface} \quad (8)$$

The charge–discharge (C–D) profile at various current densities, as shown in Fig. 4e, confirmed the ideal capacitive behaviour and excellent rate performance. Fig. 4f shows the capacitance retention of MnO_2/VGN composite for 2000 C–D cycles. The excellent charge-storage behaviour of the composite is attributed to the double-layer contribution from VGN and pseudocapacitance of MnO_2 along with the excellent electrical conductivity of the VGN as well as the hydrophilicity of the MnO_2/VGN.

Electrochemical performance of Fe_2O_3/VGN

The electrochemical performance of Fe_2O_3/VGN is investigated, while it was tested as the negative electrode (Fig. 5). A well-defined cathodic peak at −1.06 V and anodic peak at around −0.58 V are observed and they are attributed to the reversible oxidation and reduction process (Fig. 5a and S9). Along with that, a weak cathodic peak at −0.26 V and anodic peak at −0.67 V also emerged when the window is increased from 1 V to 1.35 V (Fig. 5b). These weak peaks are prominent for Fe_2O_3/VGN at lower scan rate and shown in Fig. S9. Other notable features are the reversible redox peaks are (i) shifted with respect to the scan rate for Fe_2O_3/VGN (represented by dashed line in Fig. 5a) as well as (ii) stronger and shifted when Fe_2O_3 nanorices are decorated on VGN (Fig. S9). This fact ensures that the Fe_2O_3 nanorices are well-grafted on VGN with optimized density. The possible redox reaction here is as following: [53]

$$Fe_2O_3 + 3H_2O + 2e^- \leftrightarrow 2Fe(OH)_2 + 2OH^- \quad (9)$$

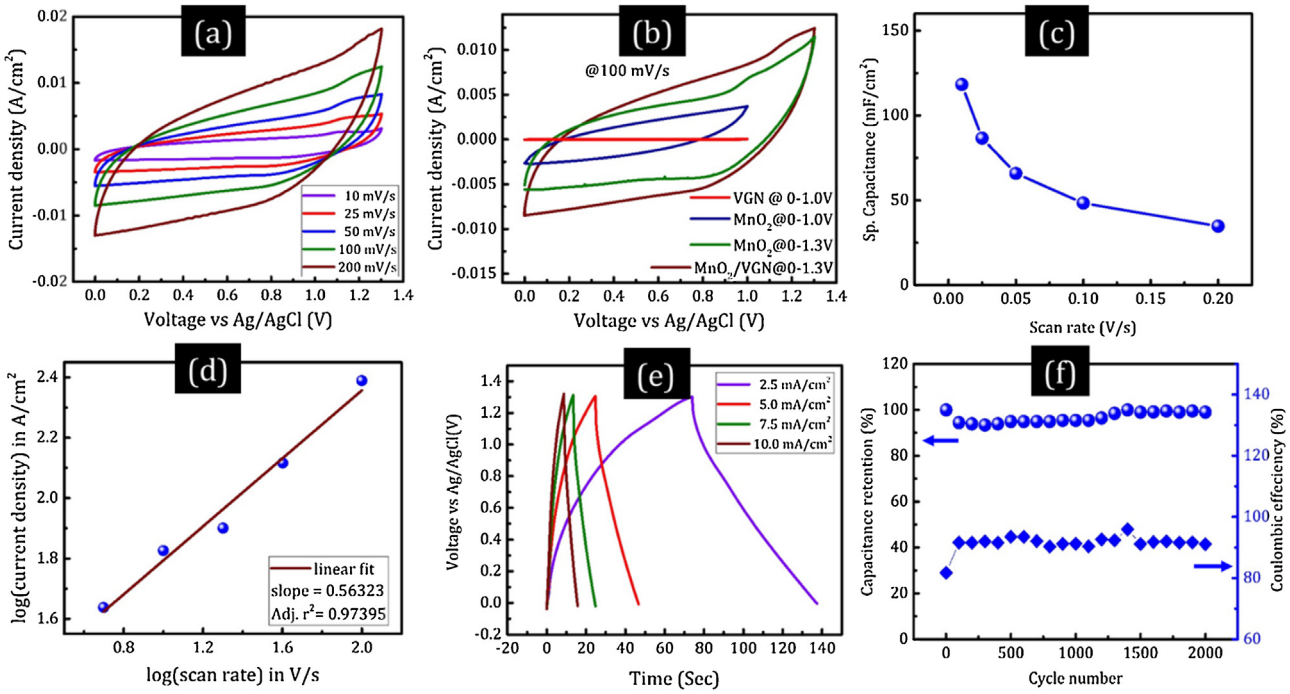

Fig. 4. (a) cyclic voltammogram at different scan rate, (b) comparative CV with respect to bare VGN and MnO_2, (c) specific capacitance with respect to scan rate, (d) current *vs* scan rate profile, (e) charge–discharge profile and (f) Capacitance retention and Coulombic efficiency with charge–discharge cycle for MnO_2/VGN electrode.

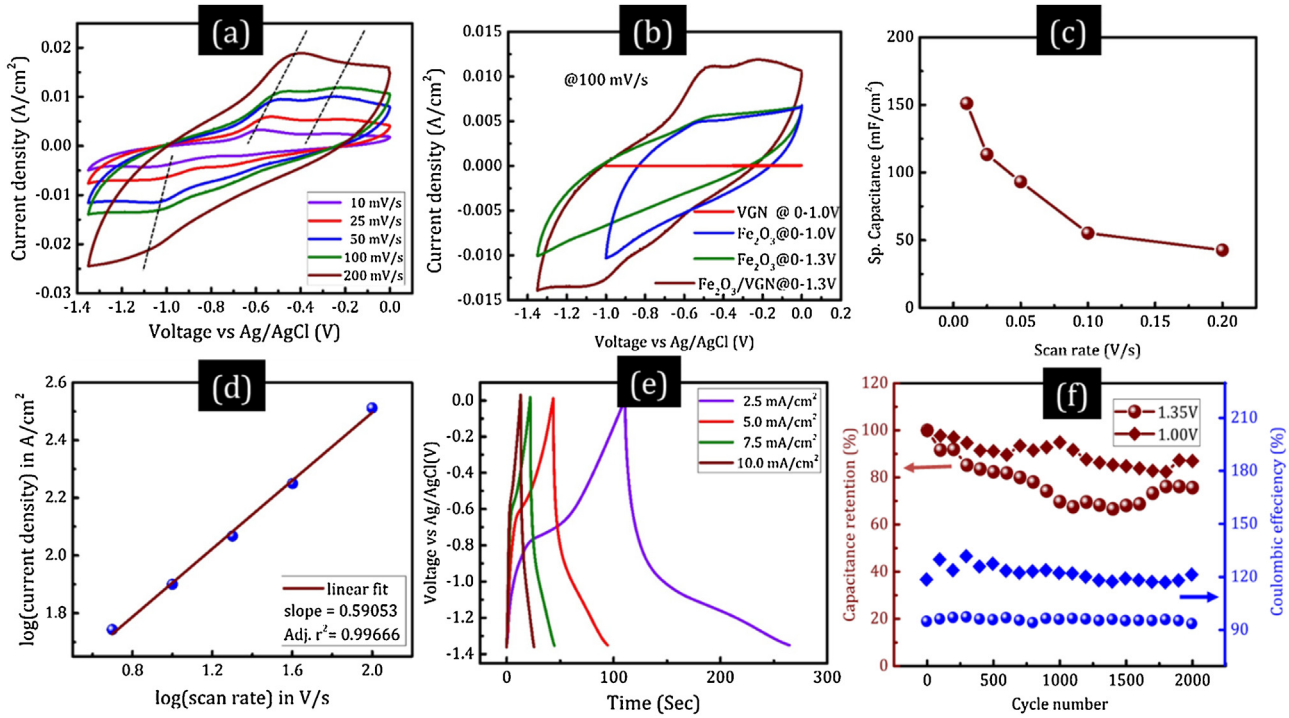

Fig. 5. (a) cyclic voltammogram at different scan rate, (b) comparative CV with respect to bare VGN and Fe_2O_3, (c) specific capacitance with respect to scan rate, (d) current vs scan rate profile, (e) charge–discharge profile, (f) Capacitance retention and Coulombic efficiency with charge–discharge cycle for Fe_2O_3/VGN electrode.

$$Fe_2O_3 + 2Na^+ + 2e^- \leftrightarrow Na_2Fe_2O_3 \quad (10)$$

$$FeOOH + H_2O + e^- \leftrightarrow Fe(OH)_2 + OH^- \quad (11)$$

The effect of Fe_2O_3 nanorice decoration onto VGN structure and thus higher charge-storage capacity is clearly observed from the comparative CV with regards to VGN and bare Fe_2O_3 nanorices (Fig. 5b). The above result also indicates the widened hydrogen evolution overpotential of Fe_2O_3/VGN and hence ability to operate the composite electrode over the potential window of 0 to −1.35 V without any hydrogen evolution [54]. The areal specific capacitance of Fe_2O_3/VGN is estimated with respect to the scan rate and plotted in Fig. 5c. The highest area-specific capacitance for the VGN is found to be 151.11 mF/cm^2 at 10 mV/s and maintained to 42.68 mF/cm^2 at 200 mV/s. The estimated capacitance of Fe_2O_3/VGN is much higher than that of graphene-wrapped Fe_2O_3 nanowire network (3.3 mF/cm^2 at 10 mV/s) [53], α-Fe_2O_3@PANI (103 mF/cm^2 at 0.5 mA/cm^2) [55], Fe_2O_3 hollow nanorod (around 80 mF/cm^2 at 10 mV/s) [56], and Fe_2O_3 nanotube annealed at 200° (~20 mF/cm^2 at 100 mV/s), 400° (~70 mF/cm^2 at 100 mV/s), 500° (~30 mF/cm^2 at 100 mV/s) and 600 °C (~15 mF/cm^2 at 100 mV/s) [57]. In our case, the Fe_2O_3/VGN was annealed at 400 °C. The areal capacitance of Fe_2O_3/VGN can be improved further by controlling the aspect ratio of nanorices and annealing temperature [57,58]. The presence of well-defined redox peaks in CV is a clear indication of the pseudocapacitive charge storage mechanism. However, to quantify its contribution, we have estimated the b-value and is found to be 0.59 as shown in Fig. 5d. Hence, like MnO_2/VGN, the semi-infinite diffusion-controlled charge storage behaviour is also confirmed for Fe_2O_3/VGN. The charge–discharge profile of Fe_2O_3/VGN, is displayed in Fig. 5e, exhibited a typical pseudocapacitive features and in good-agreement with CV profile. The higher discharge-time of the Fe_2O_3/VGN compared to its charging time is observed from its charge–discharge profile. Even, similar behaviour is also observed in the CV profile of this structure, while it scanned in more negative range. This feature is attributed to the reduction of Fe_2O_3 to metallic Fe [33]. The Fe_2O_3/VGN structure showed 75.7% capacitance retention in the potential window of 1.35 V after 2000 charge–discharge cycles, whereas 87% retention is observed when it is scanned within 1 V window (Fig. 5f). The 14.3% loss in capacitance retention after 2000 cycles is ascribed to the loss of active material due to volume change during redox reactions at the higher window [53]. However, this loss is less compared to the bare Fe_2O_3, due to good bonding with the VGN though bridging oxygen functional group.

Electrochemical performance of Asymmetric electrochemical capacitor

Considering a good charge-storage performance of MnO_2/VGN as the positive electrode and Fe_2O_3/VGN as a negative electrode, the ASC device was fabricated by sandwiching $NaClO_4$ soaked filter paper between them, which acts as a separator-cum-electrolyte reservoir. Fig. 6a shows the schematic of the ASC device fabricated. Prior to the testing of the device, charge balance between the electrodes is maintained by the area ratio of electrodes via the following relationship [56]:

$$\frac{A_+}{A_-} = \frac{C_- \times V_-}{C_+ \times V_+} \quad (12)$$

where $A_{+(-)}$, $C_{+(-)}$ and $V_{+(-)}$ are the areas, specific capacitance and the potential window of positive (negative) electrode, respectively. Thus, the calculated area ratio between the electrode is 1.32:1 for our case. The CV profile of individual electrode along with the ASC device is displayed in Fig. 6b, while scanned at 100 mV/s rate in three-electrode configuration. A series of CV tests with the different potential window is carried out in order to achieve the best operating voltage of ASC and shown in Fig. 6c. The scan rate

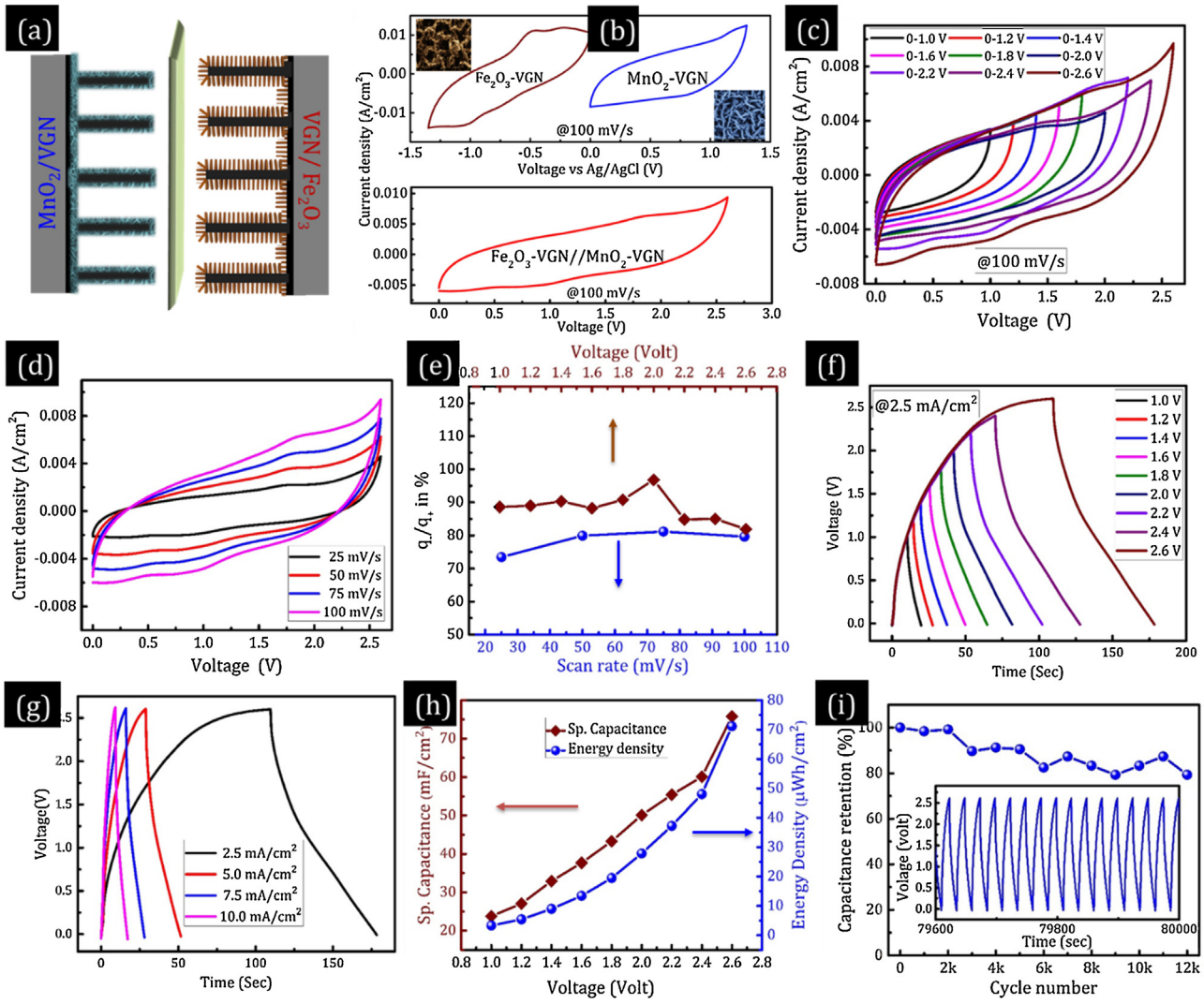

Fig. 6. (a) Schematic of Asymmetric electrochemical capacitor (ASC) device fabrication, (b) CV of individual electrodes at top and ASC at bottom; CV of ASC at different (c) potential window, and (d) scan rates; (e) Charge balance with respect to scan rate at constant window and applied voltage at constant scan rate; Charge–discharge profile at different (f) potential window and (g) current densities; (h) Specific capacitance and energy density of ASC with respect to the applied potential, (i) Cyclic stability and inset represents the intermediate cycle performance.

dependent CV result, as indicated in Fig. 6d, reveals an ideal supercapacitive behaviour. As the charge balance is one of the critical parameters for device performance, we measured the charge balance directly with the aid of GPES software. Around 90% charge-balance is observed from the experimental data (Fig. 6e). This result confirms the successful optimization of area ratio for both electrodes. However, a slight reduction in charge-balance is may be due to the water-splitting from the metal oxide and uncovered graphene surface [59]. Similar behaviour is also observed from the charge–discharge performance of the device (Fig. 6f–g). The maximum specific capacitance of ASC device is estimated to be 76 mF/cm^2 at 2.5 mA/cm^2 with 50% capacitance retention while the current density is increased by four times. Indeed, the capacitance obtained in our study is found to be much higher than that of the MoS_2/graphene symmetric cell (11 mF/cm^2 at 5 mV/s) [60], Fiber-based MnO_2/CNT/polyimide ASC (59.5 mF/cm^2 at 0.74 mA/cm^2) [61], PANI/WO3 ASC (23.2 mF/cm^2 at 0.2 mA/cm^2) [62]. The estimated energy density is calculated to be 71 μWh/cm^2 (power density = 3.25 mW/cm^2), which is around 22 times higher than that of the device while operating in 1 V (Fig. 6h). Furthermore, an excellent cyclic performance of the ASC device is confirmed as it is tested for 12,000 charge–discharge cycles with a capacitance retention of 79% (Fig. 6i). The inset of Fig. 6i is the representation of a few charge–discharge cycles.

The above result suggests the ability of the ASC device to operate at a stable cell voltage of 2.65 V. From Fig. 6(c) it is clear that the stable and safe cell voltage can be extended up to 2.6 V without oxygen evaluation in the $NaClO_4$ electrolyte. The oxygen evolution is found to be started at 2.7 V (Fig. S10). Hence, the ASC device is operated within a stable potential window of 2.6 V for further study and tested with different scan rates. The stable potential window might be caused from a synergistic effect of both positive and negative electrodes, the modified work function of active materials via chemisorption of electrolyte ions as well as extended work function difference between them (Fig. 7a).[64] Since water dissociation is limited kinetically via hydrogen/oxygen evolution on TMO surface, the stable operating voltage extended over the dissociation energy of aqueous electrolyte [65]. Only countable studies are reported on the ASC device with such high potential window of 2.6 V (Table 1).

For further understanding the charge-storage behaviour of ASC device, an impedance spectroscopy was performed in the frequency range of 100 kHz–10 mHz with an ac perturbation of 10 mV (Fig. 7b). The impedance spectra consist of semicircular arc

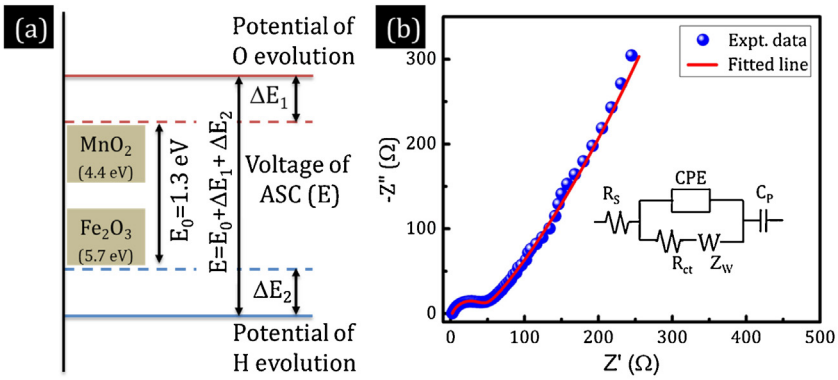

Fig. 7. (a) Schematic of the stable potential window [64] and (b) Nyquist plot of ASC.

Table 1
Summary of the highest potential window of the aqueous asymmetric electrochemical capacitor (CNF: carbon nanofiber; N-CNW: nitrogen-doped carbon nanowire; rGOA: reduced graphene oxide aerogel).

Electrode		Electrolyte	Cell voltage	Ref.
Positive	Negative			
PANI	WO_3	PVA/H_2SO_4	1.4 V	[62]
MnO_2	Graphene	PVA/LiCl	1.5 V	[42]
Graphene wrapped CNT-MnO_2	Activated carbon	1 M KOH	1.8 V	[31]
MnO_2/CNT	Fe_2O_3/CF	PVA/$LiClO_4$	2V	[33]
AgNR/rGOA	PANI NT/rGOA	PVA/H_2SO_4	1.8 V	[30]
Fe_2O_3/N-CNW	MnO_2/N-CNW	PVA/LiCl	1.6 V	[28]
Hydrogenated TiO_2 NW	MnO_2	0.5 M Na_2SO_4	2.4 V	[63]
Fiber-based MnO_2/CNT	Polyimide/CNT	CMC/Na_2SO_4 gel	2.1 V	[61]
$Na_{0.25}MnO_2$	porous carbon	1 M Na_2SO_4	2.7V	[32]
MnO_2/VGN	Fe_2O_3/VGN	1 M $NaClO_4$	2.6 V	This work

at high-frequency region accompanied with the steeper line at the lower-frequency region. The measured impedance spectra are fitted with a suitable equivalent circuit via ZSimpWin software, which is provided in the inset of Fig. 7b. Usually, an equivalent circuit for the EDLC consists of double layer capacitance (C_{dl}) in series with charge transfer resistance (R_{ct}). Since the electrode structure has varying cavity distribution, surface disorder and inhomogeneity, capacitance is replaced by constant phase element (CPE). The CPE can be expressed as $Z_{CPE} = 1/Cdl\cdot(j\omega)^n$ where j is the imaginary unit and n $(0 < n < 1)$ is related to the frequency dispersion. For the planar and smooth electrode, n equal to 1. The equivalent series resistance of device (R_s) represent the series resistance of the electrolyte, filter paper and charge barrier between the current collector and electrode materials. The Warburg resistance (Z_w), slope of 45° in the curve, is arisen due to the frequency dependent ion diffusion from the electrolyte to porous electrode surface in the intermediate frequency region. The pseudocapacitive contribution from metal oxide is represented by C_p. The R_s and R_{ct} obtained from the fitting are 2.22 and 43.67 Ω, which ensure the effective ionic/electronic transport at the electrode-electrolyte interface and good ohmic contact with the current collector. The fitted parameters for the equivalent circuit are provided in the table S1 of supporting file. The better charge-kinetics of designed ASC is the result of binder-free electrode fabrication which reduced the contact resistance. The pronounced performance of the designed ASC device is attributed to (i) large accessible surface area for the electrolyte by non-agglomerated vertical network electrode, (ii) excellent conductive pathways, (iii) superhydrophilicity of vertical TMO-graphene composite and (iv) superior electrochemical and mechanical stability.

Conclusion

A metal oxide-graphene hybrid electrode was successfully synthesized via feasible and facile techniques to fabricate an asymmetric electrochemical capacitor device. The binder-free electrodes, MnO_2- vertical graphene as the positive and Fe_2O_3-vertical graphene as the negative electrode, separated by a $NaClO_4$ soaked separator. Impressively, the fabricated Fe_2O_3–VGN//$NaClO_4$//MnO_2–VGN device showed the ability to operate with an extended window of 2.6 V. In addition to the double layer contribution, vertical graphene also supports the metal oxides structures and possess enhanced charge-storage capability. The fabricated ASC device showed a maximum capacitance of 76 mF/cm^2 with an energy density of 71 μWh/cm^2 and 79% capacitance retention over 12,000 Charge–discharge cycles. This combination of hybrid electrode materials and electrolyte endeavour with the high-performance aqueous asymmetric device showed its potential usage towards next-generation energy storage applications.

Conflicts of interest

There are no conflicts to declare.

Author contributions

S G conceived the idea, carried out the growth, data analysis and manuscript preparation. S R P and G S conducted the VGN growth and Raman spectroscopy. All authors discussed the results, commented on the manuscript, and gave approval to the final version of the manuscript.

Acknowledgement

This research was supported by Basic Science Research Program through the National Research Foundation of Korea (NRF) funded by the Ministry of Education (2018R1A4A1024691;2017R1-D1A1B03028311).

Appendix A. Supplementary data

Supplementary data associated with this article can be found, in the online version, at https://doi.org/10.1016/j.jiec.2018.12.008.

References

[1] J. Theerthagiri, G. Durai, K. Karuppasamy, P. Arunachalam, V. Elakkiya, P. Kuppusami, T. Maiyalagan, H.-S. Kim, J. Ind. Eng. Chem. 67 (2018) 12, doi:http://dx.doi.org/10.1016/j.jiec.2018.06.038.
[2] A. González, E. Goikolea, J.A. Barrena, R. Mysyk, Energy Rev. 58 (2016) 1189, doi:http://dx.doi.org/10.1016/j.rser.2015.12.249.
[3] Y. Minghao, L. Yongzhuang, Z. Haibing, L. Xihong, Chem. Eur. J. 24 (2018) 3639, doi:http://dx.doi.org/10.1002/chem.201704420.
[4] S. Ghosh, T. Mathews, B. Gupta, A. Das, N.G. Krishna, M. Kamruddin, Nano-Struct. Nano-Objects 10 (2017) 42, doi:http://dx.doi.org/10.1016/j.nanoso.2017.03.008.
[5] S. Ghosh, S.M. Jeong, S.R. Polaki, Korean J. Chem. Eng. 35 (2018) 1389, doi:http://dx.doi.org/10.1007/s11814-018-0089-6.
[6] E.M. Jin, H.J. Lee, H.-B. Jun, S.M. Jeong, Korean J. Chem. Eng. 34 (2017) 885, doi:http://dx.doi.org/10.1007/s11814-016-0323-z.
[7] V.D. Nithya, N.S. Arul, J. Power Sour. 327 (2016) 297, doi:http://dx.doi.org/10.1016/j.jpowsour.2016.07.033.
[8] S. Mitra, S. Banerjee, A. Datta, D. Chakravorty, Indian J. Phys. 90 (2016) 1019, doi:http://dx.doi.org/10.1007/s12648-016-0841-x.
[9] Q. Li, S. Zheng, Y. Xu, H. Xue, H. Pang, Chem. Eng. J. 333 (2018) 505, doi:http://dx.doi.org/10.1016/j.cej.2017.09.170.
[10] D. Sheberla, J.C. Bachman, J.S. Elias, C.-J. Sun, Y. Shao-Horn, M. Dinca, Nat. Mater. (2016), doi:http://dx.doi.org/10.1038/nmat4766.
[11] A.H. Khan, S. Ghosh, B. Pradhan, A. Dalui, L.K. Shrestha, S. Acharya, K. Ariga, Bull. Chem. Soc. Jpn. 90 (2017) 627, doi:http://dx.doi.org/10.1246/bcsj.20170043.
[12] Q. Ji, T. Yamazaki, N. Hanagata, M.V. Lee, J.P. Hill, K. Ariga, Chem. Commun. 48 (2012) 8496, doi:http://dx.doi.org/10.1039/C2CC34289H.
[13] S. Ghosh, S.R. Polaki, M. Kamruddin, S.M. Jeong, K.K. Ostrikov, J. Phys. D: Appl. Phys. 51 (2018) 145303, doi:http://dx.doi.org/10.1088/1361-6463/aab130.
[14] N.-C. Huang, Q. Ji, T. Yamazaki, W. Nakanishi, N. Hanagata, K. Ariga, S.-h. Hsu, Phys. Chem. Chem. Phys. 17 (2015) 25455, doi:http://dx.doi.org/10.1039/C5CP03483C.
[15] A.K. Sivadasan, S. Parida, S. Ghosh, R. Pandian, S. Dhara, Nanotechnology 28 (2017) 465703, doi:http://dx.doi.org/10.1088/1361-6528/aa8d90.
[16] K.K. Mishra, S. Ghosh, R.R. Thoguluva, S. Amirthapandian, M. Kamruddin, J. Phys. Chem. C 120 (2016) 25092, doi:http://dx.doi.org/10.1021/acs.jpcc.6b08754.
[17] S. Ghosh, K. Ganesan, S.R. Polaki, A.K. Sivadasan, M. Kamruddin, A.K. Tyagi, Adv. Sci. Eng. Med. 8 (2016) 146, doi:http://dx.doi.org/10.1166/asem.2016.1826.
[18] G. Sahoo, S. Ghosh, S.R. Polaki, T. Mathews, M. Kamruddin, Nanotechnology 28 (2017) 415702, doi:http://dx.doi.org/10.1088/1361-6528/aa8252.
[19] S. Ghosh, B. Gupta, K. Ganesan, A. Das, M. Kamruddin, S. Dash, A.K. Tyagi, Mater. Today Proc. 3 (2016) 1686, doi:http://dx.doi.org/10.1016/j.matpr.2016.04.060.
[20] C. Lokhande, D. Dubal, O.-S. Joo, Curr. Appl. Phys. 11 (2011) 255, doi:http://dx.doi.org/10.1016/j.cap.2010.12.001.
[21] M.D. Stoller, R.S. Ruoff, Energy Environ. Sci. 3 (2010) 1294, doi:http://dx.doi.org/10.1039/C0EE00074D.
[22] H. Tomiyasu, H. Shikata, K. Takao, N. Asanuma, S. Taruta, Y.-Y. Park, Sci. Rep. 7 (2017) 45048, doi:http://dx.doi.org/10.1038/srep45048.
[23] S. Ghosh, G. Sahoo, S.R. Polaki, N.G. Krishna, M. Kamruddin, T. Mathews, J. Appl. Phys. 122 (2017) 214902, doi:http://dx.doi.org/10.1063/1.5002748.
[24] N. Choudhary, C. Li, J. Moore, N. Nagaiah, L. Zhai, Y. Jung, J. Thomas, Adv. Mater. 29 (2017) 1605336, doi:http://dx.doi.org/10.1002/adma.201605336.
[25] J.W. Long, D. Belanger, T. Brousse, W. Sugimoto, M.B. Sassin, O. Crosnier, MRS Bull. 36 (2011) 513, doi:http://dx.doi.org/10.1557/mrs.2011.137.
[26] C. Zhu, P. Yang, D. Chao, X. Wang, X. Zhang, S. Chen, B.K. Tay, H. Huang, H. Zhang, W. Mai, Adv. Mater. 27 (2015) 4566, doi:http://dx.doi.org/10.1002/adma.201501838.
[27] G.S. Gund, D.P. Dubal, N.R. Chodankar, J.Y. Cho, P. Gomez-Romero, C. Park, C.D. Lokhande, Sci. Rep. 5 (2015) 12454, doi:http://dx.doi.org/10.1038/srep12454.
[28] W. Fu, E. Zhao, X. Ren, A. Magasinski, G. Yushin, Adv. Energy Mater. 8 (2018) 1703454, doi:http://dx.doi.org/10.1002/aenm.201703454.
[29] S. Cho, B. Patil, S. Yu, S. Ahn, J. Hwang, C. Park, K. Do, H. Ahn, Electrochim. Acta 269 (2018) 499, doi:http://dx.doi.org/10.1016/j.electacta.2018.03.020.
[30] A. Bora, K. Mohan, S. Doley, S.K. Dolui, Mater. Interfaces 10 (2018) 7996, doi:http://dx.doi.org/10.1021/acsami.7b18610.
[31] E.M. Jin, J.G. Lim, S.M. Jeong, J. Ind. Eng. Chem. 54 (2017) 421, doi:http://dx.doi.org/10.1016/j.jiec.2017.06.022.
[32] T. Xiong, T.L. Tan, L. Lu, W.S.V. Lee, J. Xue, Adv. Energy Mater. 8 (2017) 1702630, doi:http://dx.doi.org/10.1002/aenm.201702630.
[33] B. Patil, S. Ahn, S. Yu, H. Song, Y. Jeong, J.H. Kim, H. Ahn, Carbon 134 (2018) 366, doi:http://dx.doi.org/10.1016/j.carbon.2018.03.080.
[34] S. Ghosh, S.R. Polaki, N. Kumar, S. Amirthapandian, M. Kamruddin, K. Ostrikov, Beilstein J. Nanotechnol. 8 (2017) 1658, doi:http://dx.doi.org/10.3762/bjnano.8.166.
[35] K.H. Jeong, S.M. Jeong, Electrochim. Acta 108 (2013) 801, doi:http://dx.doi.org/10.1016/j.electacta.2013.07.051.
[36] X. Cheng, X. Gui, Z. Lin, Y. Zheng, M. Liu, R. Zhan, Y. Zhu, Z. Tang, J. Mater. Chem. A 3 (2015) 20927, doi:http://dx.doi.org/10.1039/C5TA03635F.
[37] Y. Zhang, Q. Zou, H.S. Hsu, S. Raina, Y. Xu, J.B. Kang, J. Chen, S. Deng, N. Xu, W.P. Kang, Mater. Interfaces 8 (2016) 7363, doi:http://dx.doi.org/10.1021/acsami.5b12652.
[38] C. Julien, M. Massot, R. Baddour-Hadjean, S. Franger, S. Bach, J.P. Pereira-Ramos, Solid State Ionics 159 (2003) 345, doi:http://dx.doi.org/10.1016/S0167-2738(03)00035-3.
[39] S. Ghosh, S.R. Polaki, P. Ajikumar, N.G. Krishna, M. Kamruddin, Indian J. Phys. 92 (2018) 337, doi:http://dx.doi.org/10.1007/s12648-017-1113-0.
[40] G. Sahoo, S.R. Polaki, S. Ghosh, N.G. Krishna, M. Kamruddin, K. Ostrikov, Energy Storage Mater. 14 (2018) 297, doi:http://dx.doi.org/10.1016/j.ensm.2018.05.011.
[41] M. Toupin, T. Brousse, D. Bélanger, Chem. Mater. 16 (2004) 3184, doi:http://dx.doi.org/10.1021/cm049649j.
[42] N. Yu, H. Yin, W. Zhang, Y. Liu, Z. Tang, M.Q. Zhu, Adv. Energy Mater. 6 (2016) 1501458, doi:http://dx.doi.org/10.1002/aenm.201501458.
[43] H. Jia, Y. Cai, J. Lin, H. Liang, J. Qi, J. Cao, J. Feng, W. Fei, Adv. Sci. 5 (2018) 1700887, doi:http://dx.doi.org/10.1002/advs.201700887.
[44] G. Sahoo, S.R. Polaki, S. Ghosh, N.G. Krishna, M. Kamruddin, J. Power Sour. 401 (2018) 37, doi:http://dx.doi.org/10.1016/j.jpowsour.2018.08.071.
[45] N.R. Chodankar, D.P. Dubal, G.S. Gund, C.D. Lokhande, J. Energy Chem. 25 (2016) 463, doi:http://dx.doi.org/10.1016/j.jechem.2016.01.020.
[46] N. Boukmouche, N. Azzouz, L. Bouchama, A. Lise Daltin, J. Paul Chopart, Y. Bouznit, Mater. Sci. Semicond. Process. 27 (2014) 233, doi:http://dx.doi.org/10.1016/j.mssp.2014.06.036.
[47] Y.E. Mendili, J.F. Bardeau, N. Randrianantoandro, A. Gourbil, J.M. Greneche, A. M. Mercier, F. Grasset, J. Raman Spectrosc. 42 (2011) 239, doi:http://dx.doi.org/10.1002/jrs.2762.
[48] T. Yamashita, P. Hayes, Appl. Surf. Sci. 254 (2008) 2441, doi:http://dx.doi.org/10.1016/j.apsusc.2007.09.063.
[49] J. Lin, H. Liang, H. Jia, S. Chen, J. Guo, J. Qi, C. Qu, J. Cao, W. Fei, J. Feng, J. Mater. Chem. A 5 (2017) 24594, doi:http://dx.doi.org/10.1039/C7TA07628B.
[50] K. Okamura, R. Inoue, T. Sebille, K. Tomono, M. Nakayama, J. Electrochem. Soc. 158 (2011) A711, doi:http://dx.doi.org/10.1149/1.3578039.
[51] J. Cao, M. Safdar, Z. Wang, J. He, J. Mater. Chem. A 1 (2013) 10024, doi:http://dx.doi.org/10.1039/C3TA12012K.
[52] L. Yuan, X.-H. Lu, X. Xiao, T. Zhai, J. Dai, F. Zhang, B. Hu, X. Wang, L. Gong, J. Chen, C. Hu, Y. Tong, J. Zhou, Z.L. Wang, ACS Nano 6 (2012) 656, doi:http://dx.doi.org/10.1021/nn2041279.
[53] H. Xuankai, Z. Haiyan, L. Na, Nanotechnology 28 (2017) 075402, doi:http://dx.doi.org/10.1088/1361-6528/aa542a.
[54] Q. Tang, W. Wang, G. Wang, J. Mater. Chem. A 3 (2015) 6662, doi:http://dx.doi.org/10.1039/C5TA00328H.
[55] X.-F. Lu, X.Y. Chen, W. Zhou, Y.-X. Tong, G.-R. Li, ACS Appl. Mater. Interfaces 7 (2015) 14843, doi:http://dx.doi.org/10.1021/acsami.5b03126.
[56] Q. Wang, X. Liang, Y. Ma, D. Zhang, Dalton Trans. 47 (2018) 7747, doi:http://dx.doi.org/10.1039/C8DT00740C.
[57] B. Sarma, A.L. Jurovitzki, Y.R. Smith, R.S. Ray, M. Misra, J. Power Sour. 272 (2014) 766, doi:http://dx.doi.org/10.1016/j.jpowsour.2014.07.022.
[58] C.C. Raj, R. Sundheep, R. Prasanth, Electrochim. Acta 176 (2015) 1214, doi:http://dx.doi.org/10.1016/j.electacta.2015.07.052.
[59] P.-C. Chen, G. Shen, Y. Shi, H. Chen, C. Zhou, ACS Nano 4 (2010) 4403, doi:http://dx.doi.org/10.1021/nn100856y.
[60] M.A. Bissett, I.A. Kinloch, R.A.W. Dryfe, ACS Appl. Mater. Interfaces 7 (2015) 17388, doi:http://dx.doi.org/10.1021/acsami.5b04672.
[61] G. Huang, Y. Zhang, L. Wang, P. Sheng, H. Peng, Carbon 125 (2017) 595, doi:http://dx.doi.org/10.1016/j.carbon.2017.09.103.
[62] Y. Zhong, Z. Chai, Z. Liang, P. Sun, W. Xie, C. Zhao, W. Mai, Mater. Interfaces 9 (2017) 34085, doi:http://dx.doi.org/10.1021/acsami.7b10334.
[63] Y. Tang, Y. Li, W. Guo, J. Wang, X. Li, S. Chen, S. Mu, Y. Zhao, F. Gao, J. Mater. Chem. A 6 (2018) 623, doi:http://dx.doi.org/10.1039/C7TA09590B.
[64] N.R. Chodankar, D.P. Dubal, A.C. Lokhande, A.M. Patil, J.H. Kim, C.D. Lokhande, Sci. Rep. 6 (2016) 39205, doi:http://dx.doi.org/10.1038/srep39205.
[65] J.-G. Wang, F. Kang, B. Wei, Prog. Mater. Sci. 74 (2015) 51, doi:http://dx.doi.org/10.1016/j.pmatsci.2015.04.003.